(Article begins on next page)

Accepted Manuscript

Modified hinged beam test on steel fabric reinforced cementitious matrix (SFRCM)

F.O. Falope, L. Lanzoni, A.M. Tarantino

Please cite this article as: Falope FO, Lanzoni L, Tarantino AM, Modified hinged beam test on steel fabric reinforced cementitious matrix (SFRCM), *Composites Part B* (2018), doi: 10.1016/j.compositesb.2018.03.019.

Modified hinged beam test on steel fabric reinforced cementitious matrix (SFRCM)

F.O. Falope[a,*], L. Lanzoni[a,b], A.M Tarantino[a]

[a]*University of Modena and Reggio Emilia, Department of Engineering Enzo Ferrari, Via P. Vivarelli 10, 41125, Modena, Italy*
[b]*University of San Marino, Via Salita alla Rocca 44, 47890, Republic of San Marino*

Abstract

An experimental campaign based on modified hinged beam test (MhBT) set-up has been reported in the present study. The samples consist of two concrete blocks coupled by a proper hinge device and laminated with steel wire fabrics embedded in a cementitious mortar layer. Two kinds of fabrics, made of galvanized steel strands with different mesh spacing, have been used to reinforce the concrete joists. With the aid of a DIC monitoring system, slippage profile at the interface between the concrete support and the mortar laminate along the contact region has been assessed, together with the fracture opening. Force vs slippage at the interface has been retrieved for the sampled tested according to the MhBT set-up. With the aim to obtain predictive ultimate load design formulas, a novel classification of laminate here proposed will be argued and related to a MhBT design formula. The influence of peel and shear stresses interaction on the ultimate strength of the system has been discussed in detail.

Keywords: FRCM, modified hinged beam test, steel fibres, slip profiles, fracture opening, ferrocement.

---

*Corresponding author
Email addresses: federicooyedeji.falope@unimore.it (F.O. Falope),
luca.lanzoni@unimore.it (L. Lanzoni), angelomarcello.tarantino@unimore.it (A.M Tarantino)

1. Introduction

The use of both long and short fibres has known a wide development in various engineering fields. This is mainly due to the high chemical and mechanical fibres properties with respect to the same bulk materials form [1, 2]. In the framework of aerospace and mechanical engineering a significant enhancement of the base materials can be obtained by exploiting nano-tube technology [3, 4, 5]. Furthermore in the field of Civil Engineering, a basic and simple technology together with a low manpower requirement have contributed to increase the demand of fibre reinforced (FR) systems. In particular, fibre-based composites are nowadays the most common material used as reinforcement and rehabilitation engagement on existing structures in the framework of civil engineering [6, 7, 8, 9].

Indeed, continuous FR composite materials are commonly used as fibre reinforced polymers (FRP) and fabric reinforced cementitious matrix (FRCM). In the case of reinforcements made of wire fabric embedded in a cementitious matrix, the composite system is generally named "ferrocement". For the FRP systems, almost always, the epoxy resin promotes the loading transfer between the matrix and the fibres. Conversely, in FRCM, the cementitious matrix allows the stress transfer to the embedded fibres.

Generally, FRP systems achieve higher mechanical performance with respect to FRCM, but this leads to relevant drawbacks, typical of polymeric materials. Fire resistance loss as well as lack of permeability, introduced by polymer matrix, make FRP unreliable materials for some European cultural heritage authority. Moreover, previous studies about the viscous effects in FRP [10] shown that epoxy-concrete interface under constant load can exhibit displacement that moving twice within few months. This relevant time-dependent effect, scoped on structures subjected to cyclic or high temperature load [11, 12, 13, 14, 15] can leads to a improper or useless repairing action. However FRCM, differently from the FRP, are significantly affected by ageing strength loss under aggressive environments which may reduce significantly the design limits [16].

2

Towards the end of the 20th century, different experimental tests have been

employed by the scientific community to investigate the bond-slip behaviour of composite materials. In particular, the available shear test schedules are subdivided in direct and indirect tests. Direct tests include the single lap set-up [17, 18, 19, 20] (Figures 1(a) and 1(b)) and the double lap test layout [21] (Figures 1(c) and 1(d)). Both single and double lap tests can be performed in near end (NE) or far end (FE) version. On the other hand, the indirect methods are the MhBT [7, 22], (Figure 1(e)) and the most common four points bending test [23, 24], Figure 1(f). The indirect tests are characterized by a more complex stress state with respect to the direct tests, which are more suitable for the calibration of the design parameters. On the other hand, indirect methods reproduce a stress state closer to that encountered in structural elements during their life.

In order to connect the results provided by direct and indirect tests, a numerical FE simulation based on non-linear fracture mechanics theory was performed by [25], investigating the differences induced on the stress state by single, double lap and beam tests. It's shown that, although of single and double lap tests provide similar results, the MhBT provides higher ultimate bond strength values.

The load transfer mechanism between the matrix and fabric plays a crucial role in the design of composite structures. The investigation of the transfer mechanism has led the scientific community to carry out extensive experimental programs to better understand the interfacial stress distribution and its dependence on the geometric and material parameters.

The experimental programs performed in literature pointed out that the crack initiation at the nearest loading point shifts the active bonded zone toward a new region farther from the loading point. The bond activation zone plays a crucial rule, for which it has been introduced the concept of a characteristic length, named effective or transfer length L_e, beyond which the load transfer capability become negligible. A definition of the effective bond length as the region in which the strain assumes a linear distribution was proposed in [22].

3

(a) Single lap in far end (FE) version.

(b) Single lap in near end (NE) version.

(c) Double lap in far end (FE) version.

(d) Double lap in near end (NE) version.

(e) Modified hinged beam test (MhBT).
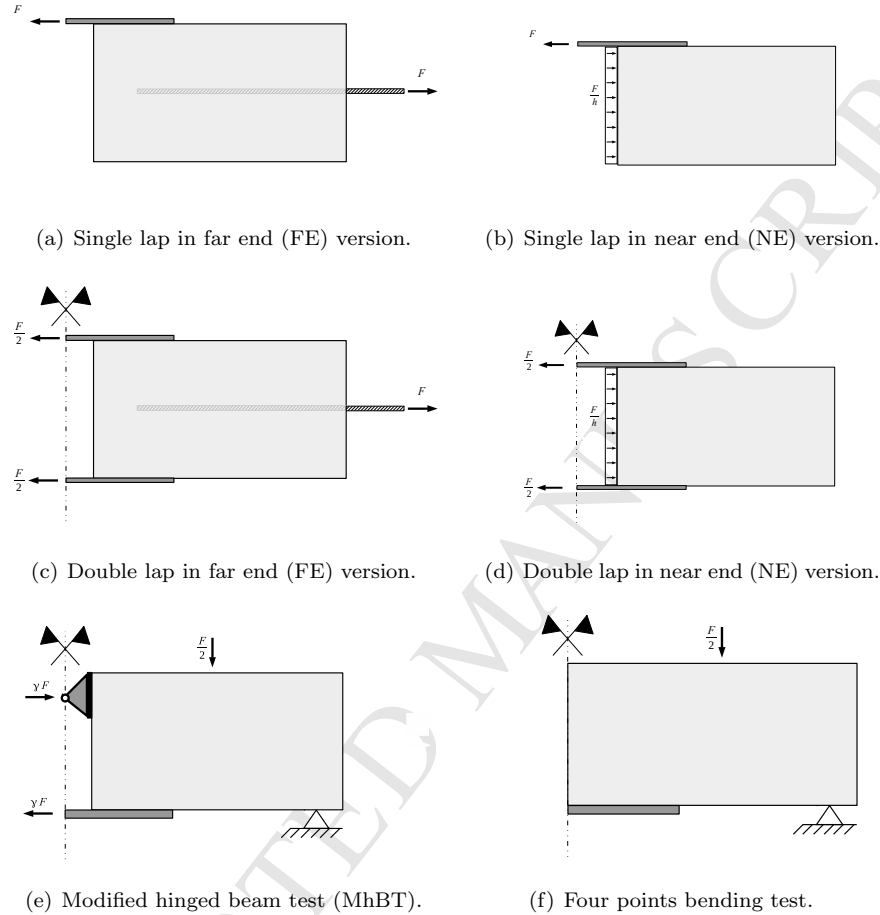
(f) Four points bending test.

Figure 1: Available bond tests schedules.

⁶² Differently, in [26] the effective bond length was denoted as the length needed to attain the 97% of the ultimate load depending on the assumed bond-slip ⁶⁴ relationship provided by an assumed theoretical interface constitutive models.

As reported in [27], the monitoring of the shear tests by using conventional ⁶⁶ strain gauges does not provide sufficient information to grasp local phenomena and high strain levels which typically occur in the neighbourhood of the lam- ⁶⁸ inate edges. Conversely, the use of full-field monitoring methods are suitable to properly describe local effects. In particular, the constant growth of non-

4

destructive technologies based on optical physics for surface field monitoring allows a higher resolution description of the delamination process. A far-field airbone Radar (FAR) technique has been used in [28] to analyse the influence of humidity and temperature on debonding phenomenon in FRP specimens subjected to four points bending test. Digital image correlation (DIC) instrumentation allows monitoring the fracture opening in a NE single lap test to capture the evolution of the interfacial stress distribution as the external load increases [29]. Conversely, the use of full-field monitoring methods are suitable to properly describe local effects. In particular, the constant growth of non-destructive technologies based on optical physics for surface field monitoring allows an higher resolution description of the delamination process.

The present paper deals with the bond behaviour of FRCM laminated on a concrete support through a MhBT. The test program aims to the discussion of the reliability, in terms of unwanted and encountered failure mode, of the MhBT set-up. In addition, the possibility of this set-up to be performed on specimens with reduced span length, with respect to the original structural element, should be make this test particularly suitable for the bond test on existing structural element. The test is performed by recording the load vs deflection, under the upper knives, up to the sample failure. In order to investigate the monitored fracture opening, for which an analytical treatment can be found in [12, 30] and [31, 32], for infinitesimal and finite elasticity theory, respectively, DIC monitoring has been used to investigate the slip at the interface as well as fracture growth within the contact region. The paper is organized as follows: Sec 2 describes the specimen and test schedule design based on the materials characterization, as well as the test variables. The results are discussed in Sec.3 in terms of force-displacement response and DIC post-processed slip fields. The force-displacement result, supported by the DIC monitoring, allow to understand the effect of lamination length in terms of global results, force-displacement ultimate values and failure mode, as well as the local results, slip profiles and fracture opening. A design formula has been used to predict the ultimate load as a function of the failure mode strictly connected to the fab-

5

ric used. The influence of the peeling stress, generally neglected in theoretical
model, will be treated in Sec 4, by considering the analytical model of a beam
bonded to an elastic half-plane [33, 34].

2. Experimental program

2.1. Research significance

The experimental program carried out in the present study has been organized to investigate the following issues:

- analyse the load transfer capability of two different types of unidirectional steel fabrics (Figure 2(a)) laminated on a groove grid concrete support (Figure 2(b));

- evaluate the capability of the MhBT to run as reference test for characterization of reinforcing and rehabilitation engagements on existing structures owing to its wide adaptability both in terms of set-up arrangement and in particular cases the sample number could be increased. Indeed starting from two existing beam elements of 1.5m length, the MhBT allows to carry out three tests instead of two, by the beams cutting into three portions of 50cm length, in order to obtain three specimens realized from the union of two 50cm beams block (as described in Section 2.2 and performed in [7]). In addition, considering as an acceptable specimen block length 50cm, the hinge presence, which length is about 8cm, allows to earn an important length compared to the entire specimen. In the field of the existing building structural element the sample number increase could represent a relevant aspect. Particular attention will be paid to analyse how vacuum thrust, an unwanted failure not encountered in the original state of the manufacture, can influence the beam-test results;

- identify the serviceability load and the optimal lamination length over which the load can be bear without exhibit crack patterns [30, 35];

6

128 • discuss the external work $\mathcal{L}_{e,\tau}$, related to the failure of the interface and defined as the area under the force-slip plot $(P - \delta)$.
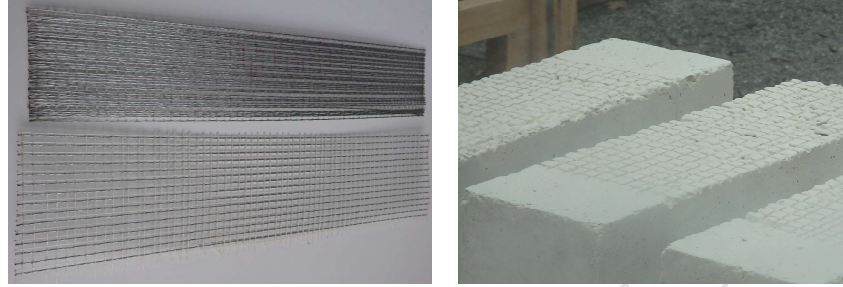
(a) From top to the bottom, wire fabric A and C

(b) Surface groove grid

Figure 2: Steel fabric and surface treatment.

2.2. Experimental schedule and specimens design

130

A total of 24 specimens have been tested through MhBT schedule up to 132 failure. Each specimen consists of two prismatic concrete blocks coupled by a mechanical hinge device placed at the upper part of the cross sections as 134 shown in Figure 3(a). This schedule inspired to [36], born for longitudinal steel reinforcement bond test, is particular useful since both the compression and 136 tension resultant magnitude and position are known during the test.

Two test variables have been considered. The first one is the lamination 138 length (L_A), which denotes the length of the composite contact region for each block. The following effective bond length formulas, given by [23],

$$L_e = \sqrt{\frac{E_f t_f}{2 f_{ctm}}} = 30 \ cm,$$

140 has been initially adopted to set the lamination length limits, where E_f, t_f and f_{ctm} are the fibre Young modulus, ultimate tensile mean strength (Table1) 142 and the concrete ultimate tensile mean strength (Table2), respectively. It has been decided to investigate the behaviour of three different specimen groups for 144 each type of wire fabric by choosing three different lamination lengths, equal

7

to 10, 20 and 30 cm. The second variable is represented by two unidirectional

wire fabrics characterized by different mesh spacings. These fabrics are made of galvanized steel strands, named type A and C fabric, Figure 2(a), which differ in the wire mesh spacing over the fabric section (A_f) fixed the support width (b), as reported in Table (1). Each specimen has been labelled with a code representative of fabric type, lamination length and identification number in the specimen group (e.g A_{24}, represents the fourth specimen with 20 cm lamination length made with wire fabric A).

The test set-up geometries aim to simulate elements representative of structural beams or slab joists sawed from an existing structure, as carried out in [7]. All blocks have a rectangular cross section 15 cm width, 28 cm heigh (h) and 50 cm long (L). During the concrete caste, each block has been reinforced with longitudinal steel bars ($f_u = 450$ MPa) of 6 mm diameter and 2 cm cover, placed at both upper and lower sides of the cross sections. Transverse steel shear reinforcements with double bracket, 15 cm longitudinally spaced, have been inserted in each concrete block, Figure 3(c).

In order to promote adhesion between the laminate and the substrate, after 14 days curing, a groove grating with a square mesh of 1.5×1.5 cm and 4 mm depth, see Figure 2(b), has been realized on the lower surface of each block. The specimens have been composed by coupling two blocks with a hinge device, placed at the upper side of the cross section and fixed by means of proper mechanical inserts, as shown in Figures 3.

Once the block pairs have been realized, the specimen intrados has been wetted and a first thin cementitious mortar layer 4 mm height (t) was laid on the block surface for a chosen lamination length. The steel fabric has been applied on the mortar bed (still wetted) and the laminate has been completed with a second mortar layer similar to the previous one. The attitude of the composite layer to prevent delamination process is provided by the fabric wire mesh, which confers higher internal grip to the laminate. After 28 days, once the laminate has been cured, the specimens have been tested through a bending test, according to Figure 3(a).

8
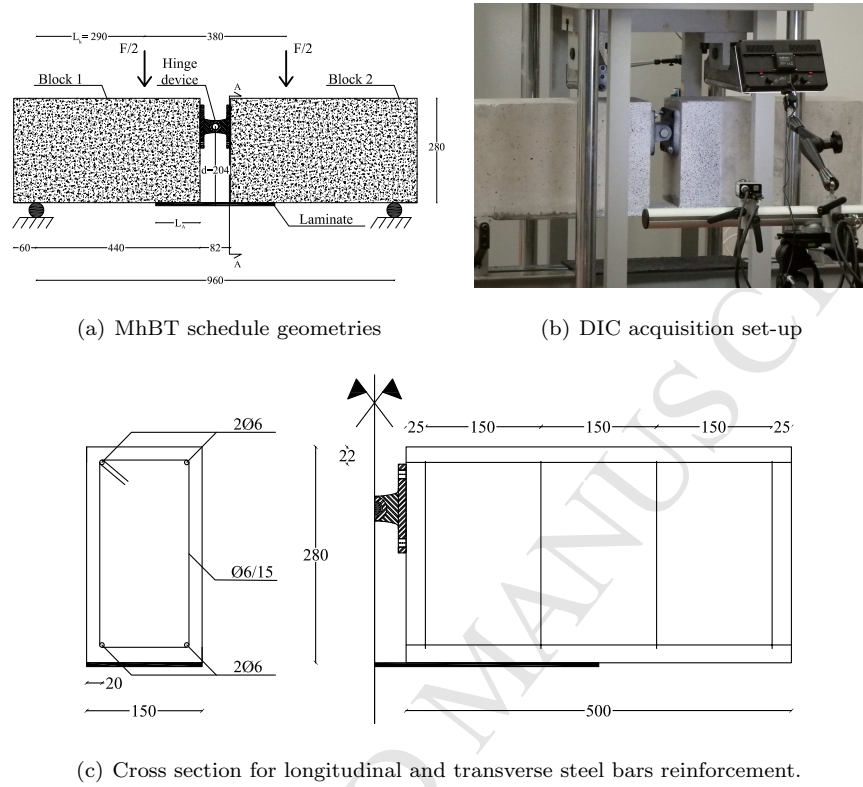
(a) MhBT schedule geometries

(b) DIC acquisition set-up

(c) Cross section for longitudinal and transverse steel bars reinforcement.

Figure 3: Test set-up, units [mm].

2.3. Materials characterization

In addition to the block pairs, six cubic samples of 15 cm size have been cast in order to measure the concrete compressive strength (R_{cm}) from which the concrete tensile strength (f_{ctm}) has been inferred (Table 2) according to [37]. In addition six $4 \times 4 \times 16$ cm prismatic samples of laminate cementitious

Type	ρ [g m^{-2}]	A_f/b [mm^2 cm^{-1}]	t_f [mm]	f_u [MPa]	ε_u [%]	E_f [GPa]
A	2000	4.72	0.084	2900	1.4	205
C	600	1.57				

Table 1: Galvanized steel fabric geometries and single strands mechanical properties.

9

	b [mm]	h [mm]	E [GPa]	R_{cm} [MPa]	f_{ctm} [MPa]
Laminate cementitious mortar	150	4+4	25	37.5($\pm$9.46)	8.86($\pm$5.27)
Concrete support	150	280	25	18.93($\pm$12.9)	1.88($\pm$8.64)

Table 2: Mortar laminate and concrete support properties.

mortar have been tested through three points bending test and compression
182 test in order to assess the Young modulus (E), mean compressive strength and
tensile strength (Table 2) according to [38]. The rough wire fabric, according to
184 [39], has been characterized under tensile test, f_u, ε_u and E, i.e. the ultimate
tensile stress, the ultimate strain and the Young modulus, respectively. The
186 mean values provided by the experimental test have been reported in Table 1.

2.4. MhBT load and monitoring procedures

188   The laminated specimen pairs have been tested in a four-points bending
test using a MetroCom 7170S02 machine equipped with a 200 kN load cell
190 with 0.6 kN resolution. The test has been performed according to 1 mm/min
displacement rate. The machine has been equipped with a LVDT (linear variable
192 displacement transducer) to monitor the deflection at the loading point. For
some specimens, the displacement field in the neighbourhood of the sample
194 midspan has been acquired through a DIC instrumentation (Figure 3(b)) in
order to grasp slip at the support-laminate or laminate layer interface. The
196 specimens that have not been acquired with DIC have a slash symbol in Table 3
under DIC amounts. DIC has been calibrated in order to acquire a 30×30 cm
198 square window, centred at the middle span of the specimen. The acquisition
system configuration ensures 10 μm resolution.
200   In order to measure the substrate-laminate or laminate layers interface slip,
DIC displacement field has been referred to horizontal reference lines L_1 and
202 L_2 oriented with the x axis, as sketched in Figure 4, placed in correspondence
of the first and second thin mortar laminate layer, respectively. During the
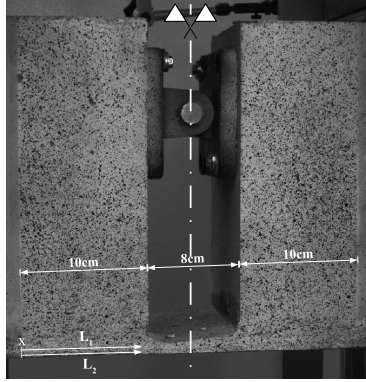
10

Figure 4: DIC reference system and reference lines.

²⁰⁴ loading phase, the gap between the horizontal displacements of the reference lines provides the slip distribution along the sample. Note that a third reference ²⁰⁶ line placed on the support over and parallel to L_1 should be required to evaluate laminate-substrate slip. Moreover, as discussed in Section 3, the groove grid ²⁰⁸ realized on the support intrados before lamination provides a strong anchor system, hence no slip occurs at the support-laminate interface.

3. Results and Discussion

3.1. Force displacement results and failure modes

²¹² The MhBT results have been reported in Figure 5 for different types of wire fabrics. The detailed results for each type of wire fabric have been reported ²¹⁴ in Tables 3 and 4 in terms of the following quantities: maximum vertical force (F_{MAX}), vertical displacement corresponding to F_{MAX} (v_{MAX}), fibre maximum ²¹⁶ stress ($\sigma_{f,MAX} = P_{MAX}/A_f$), where P_{MAX} is the maximum tensile force on the fabric. It should be noted that the symbol F will be used in the following to ²¹⁸ denote the vertical resultant force applied by the upper knives, differently from the symbol P that denotes the force acting on the laminate evaluated as,

$$P = \frac{FL_k}{2d}$$

11

220 where L_k and d, represent distance between the upper and lower knives and the internal lever arm (Figure 3(a)). Moreover the overline symbol will be used to 222 denote mean amounts of the entire specimens group. In addition, the DIC post processed data have been reported in Tables 3 and 4 in terms of maximum slip 224 between the laminate layers (δ_u), external work $(\mathcal{L}_{e,\tau})$ and the relative error $\epsilon_{P_{MAX}}$ (defined from eq 3) for the estimation of the maximum tensile fibre force 226 with respect to a theoretical predictive design formula eq 2.

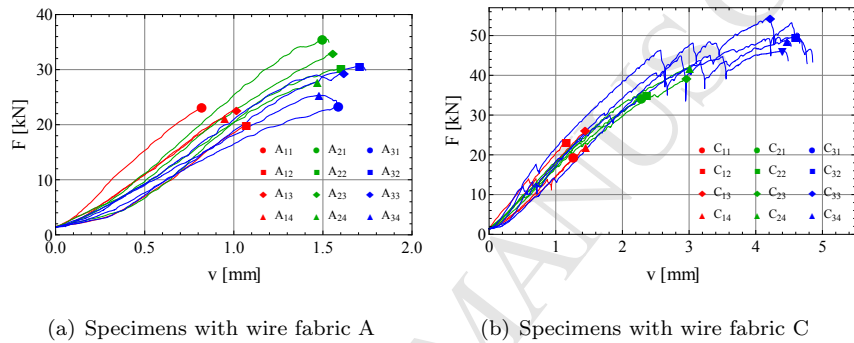(a) Specimens with wire fabric A   (b) Specimens with wire fabric C

Figure 5: Beam-test force displacement results.

As reported in Figure 5 for specimens C, as the lamination length increases, 228 the maximum load increases tending to a plateau. For the specimens C, the lamination length affects both the maximum strength and displacement. A 230 different result has been provided by specimen A, where over the 20 cm lamination length, the maximum displacement are nearly the same while the maximum 232 force decreases. Because of its larger mesh size, the wire fabric C provides high mechanical interaction between the laminate layers. As a consequence of the 234 increase in shear transmission capability, both the maximum force and displacement increase with the lamination length, Figure 6. In the region close to the 236 laminate edges the stress level grows with the external load. The stress redistribution, related to the longitudinal displacement field contour map in Figure 7, 238 paints the activation of a more extended concrete reacting zone for specimen C with respect to the specimens A. A longer lamination length, for specimens C, 240 implies a longer reacting region along the interface and, in turn, more compres-

12

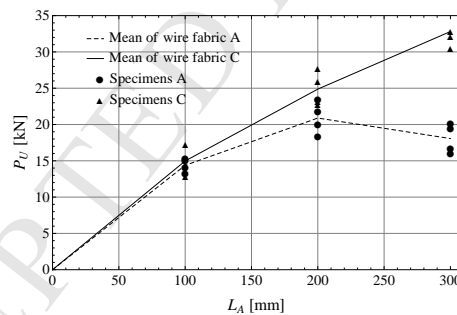| L_A [mm]	Spec	v_{MAX} [mm]	F_{MAX} [kN]	σ_{fu} [MPa]	δ_u [mm]	$\mathcal{L}_{e,t}$ [kJ]
100	1	0.81	23.17	405.65	/	/
	2	1.07	20.03	350.55	/	/
	3	1.01	22.75	396.27	0.06	0.66
	4	0.95	21.28	372.49	0.10	0.78
200	1	1.53	35.55	622.26	/	/
	2	1.60	30.39	532.02	0.26	3.22
	3	1.56	32.97	577.12	0.64	5.59
	4	1.46	27.85	487.44	/	/
300	1	1.58	23.49	411.14	0.11	1.01
	2	1.73	30.62	535.92	0.13	2.35
	3	1.63	29.44	515.37	/	/
	4	1.58	25.34	443.64	0.16	2.66

Table 3: Results for wire fabric type A

Figure 6: Effect of lamination length, maximum load with anchored length.

sive trusses inside the concrete samples, according to the Morsch scheme.

A summary of mean maximum load $(\overline{F}_{MAX})$, coefficient of variation (CV) and the mean fibre employment index, defined as the ratio between the mean fibre maximum stress over tensile fibre strength $(\overline{\sigma}_{f,MAX}/f_u)$, have been reported in Table 5 for each specimen group. As highlighted by the employment index, fabric C achieved a stress level nearly close to its ultimate stress, conversely to

13

L_A [mm]	Spec	v_{MAX} [mm]	F_{MAX} [kN]	σ_{fu} [MPa]	ϵ_{P_u} [%]
100	1	1.26	19.38	1032.65	-19.29
	2	1.16	23.20	1235.73	-42.8
	3	1.45	26.25	1398.42	-61.58
	4	1.45	22.05	1175.00	-35.73
200	1	2.28	34.45	1835.07	5.75
	2	2.39	35.18	1874.11	3.76
	3	2.96	39.32	2094.55	-7.57
	4	3.01	41.99	2236.33	-14.87
300	1	4.77	49.73	2649.01	5.81
	2	4.85	54.45	2900.58	-3.13
	3	4.52	48.75	2596.82	7.67
	4	4.48	46.15	2458.22	12.59

Table 4: Results for wire fabric C

(a) A_{22} (b) C_{23}
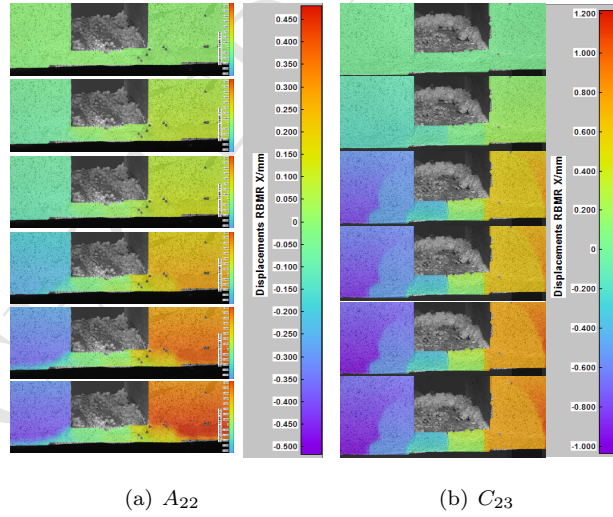
Figure 7: Longitudinal DIC displacement field u at different load levels, respectively 0.1, 0.4, 0.5, 0.85, 0.95 0.99 P_u.

Group	$\overline{v}_u$ [mm]	$\overline{F}_{MAX}$ [kN]	$\overline{\sigma}_{f,MAX}/f_u$
A_1	0.96 ($\pm$11.6)	21.81 ($\pm$6.58)	0.13
A_2	1.54 ($\pm$3.84)	31.69 ($\pm$10.46)	0.19
A_3	1.63 ($\pm$4.34)	27.22 ($\pm$12.35)	0.16
C_1	1.33 ($\pm$10.86)	22.72 ($\pm$12.53)	0.42
C_2	2.66 ($\pm$14.23)	37.74 ($\pm$9.42)	0.69
C_3	4.66 ($\pm$3.92)	49.77 ($\pm$6.96)	0.91

Table 5: Mean $\pm$ CV [%] result and fibre strength optimization index.

the fabric A, in which the achieved stress is significantly lower.

²⁴⁸ Three different failure modes have been observed. An adhesive failure (AF) ([40]) has been found for the wire fabric A, Figures 8(a) and 8(b), owing to ²⁵⁰ a progressive fracture propagation along the lower plane of the fabric. This type of failure is due to low mechanical grip induced by the small mesh size. ²⁵² Conversely, for specimens C failure occurred because of high stress level transferred from the laminate into the concrete support. In particular, in the case ²⁵⁴ of C_1 specimens, failure was due to vacuum thrust (VT) generate by shearing stress in the neighbourhood of the block edge, with a consequent detachment ²⁵⁶ of the concrete, as shown in Figure 8(d). Indeed, the concrete corner was subjected to stress concentration, and the increase of lamination length, for C_2 and ²⁵⁸ C_3 group, has led to concrete shearing failure driven by crack formation and propagation starting from the laminate ends, Figures 8(e) and 8(f). For C_2 ²⁶⁰ specimens, crack propagation started from the laminate up to the intersection of the lower longitudinal steel reinforcement. Instead, for C_3 group, failure has ²⁶² been caused by crack propagation starting from the laminate which joins the compressive region. The higher load transfer capability of fabric C is evidenced ²⁶⁴ by the load-displacement curve.

Each specimen C has exhibited a sudden loss and recovery in carry capacity ²⁶⁶ before failure, as displayed in Figure 5. This response is related to progressive crack formations at the midspan of the laminate layer, highlighted as the lami-
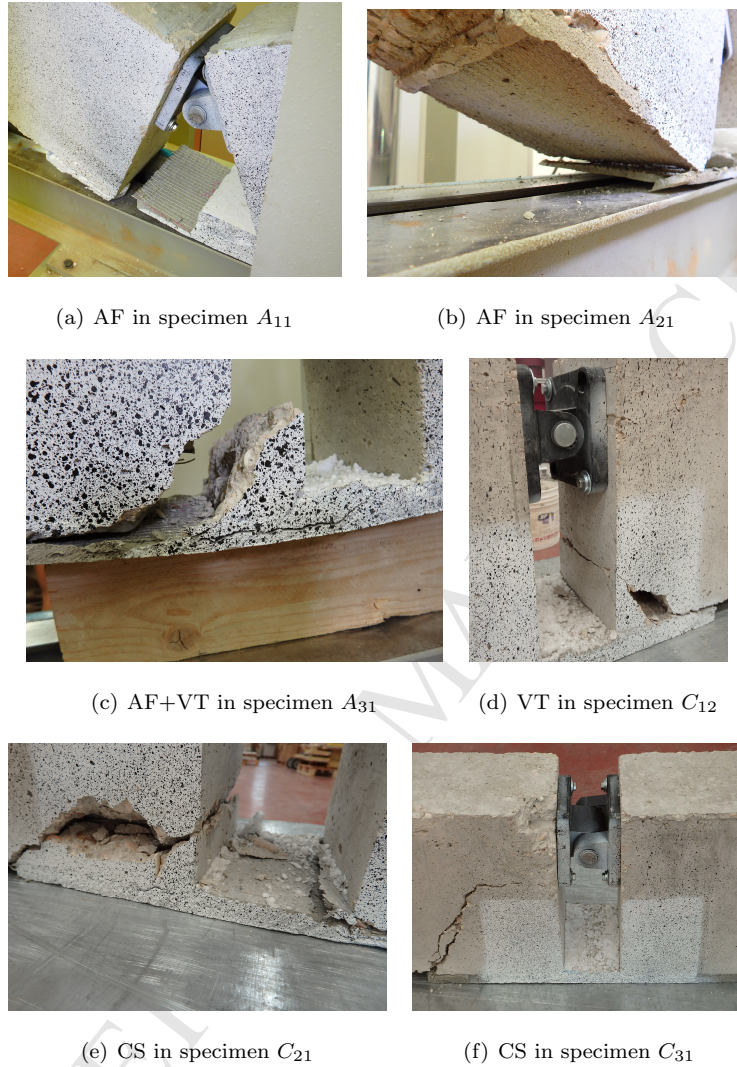
(a) AF in specimen A_{11}

(b) AF in specimen A_{21}

(c) AF+VT in specimen A_{31}

(d) VT in specimen C_{12}

(e) CS in specimen C_{21}

(f) CS in specimen C_{31}

Figure 8: Failure mode: adhesive failure (AF), concrete shearing (CS) and vacuum thrust (VT).

nation length increase. This behaviour has not been observed in specimens A, where the system tends to dissipate energy through cracks propagation along the interface between fabric-mortar support.

16

3.2. Slip profiles, bond slip-relation and interface shear energy

272 Making reference to the system shown in Figure 4, the displacement component x along the L_1 and L_2 reference lines, respectively u_{L_1} and u_{L_2}, have been
274 acquired by DIC optical system. As no cracks occur at the interface between support and laminate, only adhesive slip has been observed. Accordingly, the
276 slip between the laminate layers has been calculated as follows

$$\delta(x) \quad = \quad u_{L_2}(x) - u_{L_1}(x).$$

The slip distribution has been assessed based on the difference of spline fitting
278 on the displacement field provided by DIC along the aforementioned reference lines. The characteristic slip distributions have been reported in Figure 9 at
280 different load levels for specimens A_{13}, A_{22} and A_{31}, representative of their own group behaviour. In addition, the slip profile of specimen A_{23} has been reported
282 to better understand local phenomena observed and discussed in Section 3.3, as well as for two C specimens, to proof that no slip occurred for fabric C,
284 Figures 9(e) and 9(f). For the sake of clarity, two vertical lines have been introduced in Figures 9 corresponding to the hinge ends. A stronger skew-
286 symmetric slip profile shown by Figure 9(a) has been found for specimen A_{13} with respect to specimen A_{22} and A_{31} which shown skew trend in the initial
288 load phases only, 9(b) and 9(d). For specimen A_{23} a different failure mechanism has been observed. The specimens C have not exhibited slip. As shown by
290 Figures 9(e) and 9(f), the slip was caused by fracture phenomena localized in the neighbourhood of the blocks edges or near the hinge only. Conversely,
292 for fabric A the slip increases with the load, reaching its maximum value in the neighbourhood of the block corners from which it propagates. For each
294 specimen A, the maximum slip has been reported in Table 3.

In this study, slip has been computed as the relative displacement between
296 L_1 and L_2 at the laminate lateral edge. Typically for the case of single lap test, the slip has been calculated by the use of LVDT placed at the upper surface
298 of the laminate layer, where the acquired displacement became slip through the assumption of a fixed support. The lateral monitoring grasps exactly the
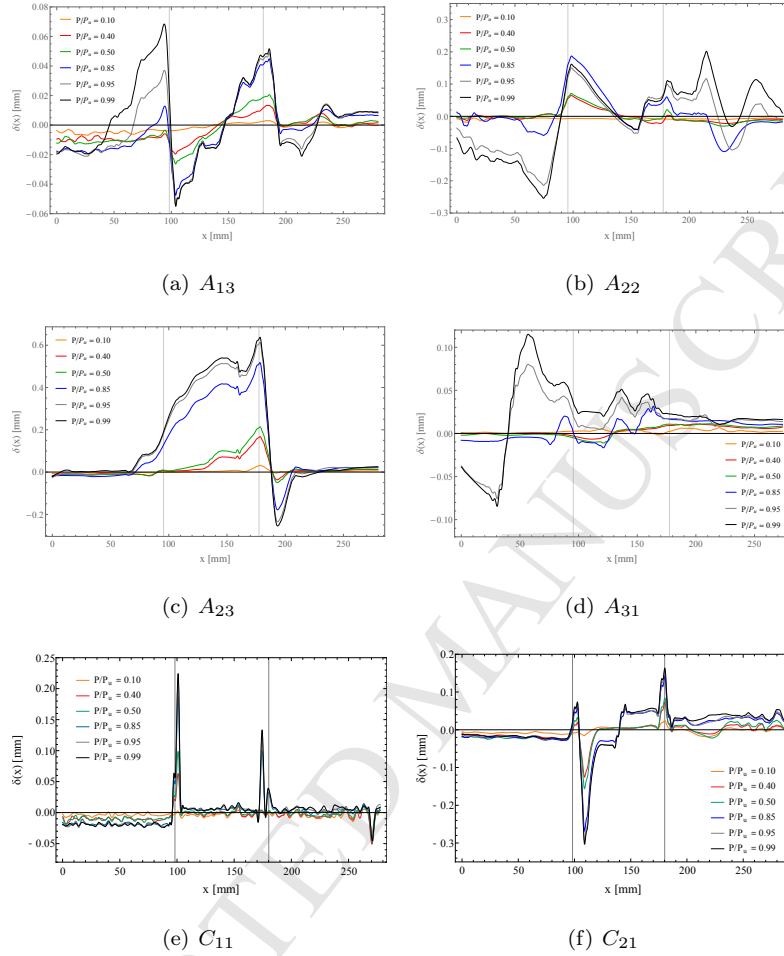
17

Figure 9: Slip profiles provided by DIC post-processing data referred to the reference lines.

³⁰⁰ relative slip profile definition but only on the lateral surface, while the upper surface slip monitoring allow to describe the slip profile anywhere. However ³⁰² this monitoring technique is incapable to distinguish laminate-support or inner laminate layers slip.

³⁰⁴ The local constitutive bond-slip relation affects the delamination phenomenon. Based on the assumptions of linear elastic behaviour of the concrete matrix, ³⁰⁶ negligible laminate bending stiffness and peeling stress and assuming uniform distribution of the normal stress across the laminate cross section, the follow-

18

308 ing second order differential equation is found from the laminate and support equilibrium and compatibility condition [26, 41],

$$\frac{d^2\delta(x)}{dx^2} - \Omega\tau(x) = 0, \tag{1}$$

310 where Ω represents the stiffness parameter of the system ($\Omega = \frac{1}{E_f t_f} + \frac{b_f}{b_s E_s t_s}$ or $\frac{2b_f}{E_f A_f}$ respectively from [26] and [41] where E_f, A_f and t_f represent the 312 Young modulus, cross section area and thickness of the fabric, respectively). The determination of stress, strain and displacement fields are based on the 314 statement of a global $\tau(\delta)$ constitutive law. Different laws have been widely investigate by [26] for FRP composite, starting from the assumption of linear, 316 multi-linear or multi-linear combined with exponential decay $\tau - \delta$ relations.

Differently from the direct tests, in the MhBT set-up the peeling stress 318 component becomes relevant and the approach proposed by [26] should be badly grounded. So the external work has been calculated as a measure of the ductility 320 of the system,

$$\mathcal{L}_{e,\tau} = \int_0^{\delta_u} P d\delta.$$

The experimental force-slip curves provided by DIC post-processing have been 322 obtained fixing the x coordinate where the slip profile reaches its maximum (Figure 9) with the associate monitored load absorbed by the laminate. The force-slip curves have been reported in Figure 10. The obtained results show that
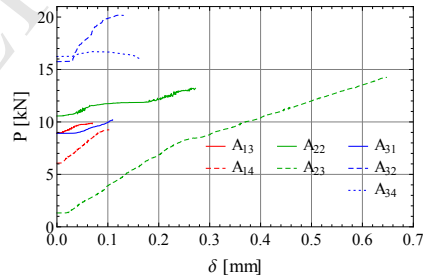

Figure 10: DIC bond-slip post-processing results.

324

the force increases almost linearly with the slippage, displaying an ascending

19

₃₂₆ trend after an initial plateau. With particular attention to the specimen A_{22} and the singular A_{23} behaviour, despite of different values in the term of the ₃₂₈ ultimate displacement, the external work reproduces the same attitude of the system to dissipate energy.

₃₃₀ *3.3. Crack opening*

For the case of specimen A, in order to establish a critical load threshold ₃₃₂ over which crack occurs at the interface between the laminate layers, the crack opening plots have been reported in Figure 11. These plots have been referred

(a) A_{13}

(b) A_{22}

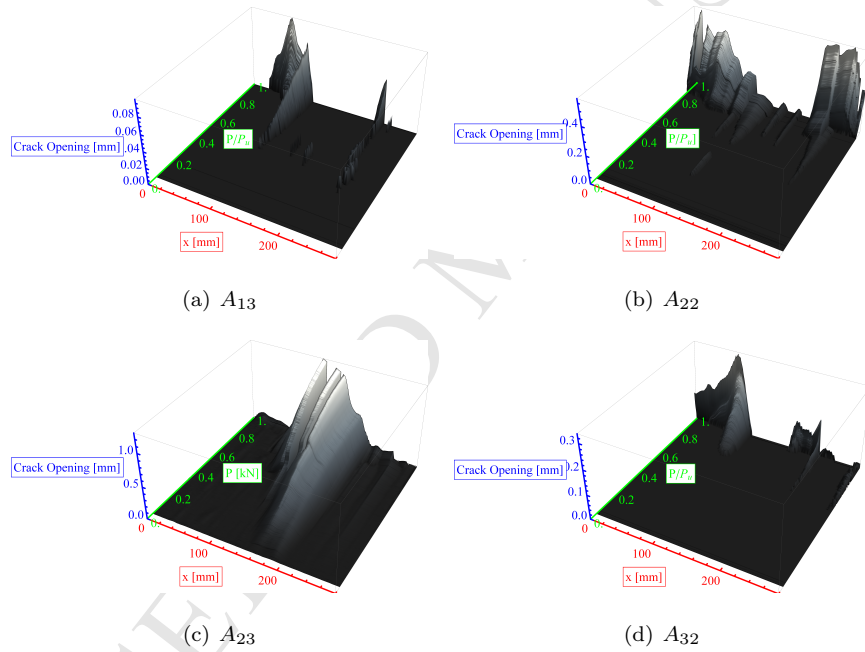(c) A_{23}

(d) A_{32}

Figure 11: Crack propagation.

₃₃₄ to the spatial coordinate system of Figure 4 and the ratio between the actual load and the ultimate load. The fracture opening has been obtained as the ₃₃₆ difference between the reference lines vertical displacements amongst which the fracture propagates,

$$v_{crack}(x, F) \quad = \quad v_{L_2}(x, F) - v_{L_1}(x, F).$$

20

With the exception of specimen A_{23}, an almost homogeneous and congruent behaviour is retrieved for specimens belonging at the same group. As the lamination length increases, the load threshold characterizing the crack formation increases. For specimens A_{13} and A_{22} the effect provided by the lamination length is more pronounced on the magnitude of the crack opening than the load level corresponding to crack formation. The increase of dissipation capability of the system is enforced by the external work grow, Table 3. Whereas for A_{13} and A_{22} the crack propagation started at 0.5-0.6 P_u, for sample A_3 the critical load shifted over 0.7 P_u. Moreover, for specimens A_3 the advantage provided by increasing the lamination length in terms of crack formation is paid in terms of dissipated energy which comes back closer to the values exhibited by sample A_1. Differently from the previous cases, specimen A_{23} has shown a congruent global behaviour with respect to its group, but showing an anomalous local phenomenon. Indeed, sample A_{23} has exhibited a delamination process coupled with a leveraging effect induced by the right block corner. Pushing of the right block corner on the laminate induces an early crack formation. Figure 9(c) shows that, for this specimen, slippage has occurred at higher magnitude and earlier load level compared to the sample A_{22}. Slippage recovered for specimen A_{23} is related to a counter-clockwise rotation induced by this phenomenon localized near the corners of the block. However, based on data listed in Table 3 and shown in Figure 10 it is remarked that, even if such a local phenomena occurs, external work does not significantly change.

3.4. Design consideration

As shown in the previous Sections, a high strength and rigid interface, such as the one provided by the fabric C, leads to a shearing failure in the concrete support. The design of FRCM system bonded to a concrete support mainly depends on the attitude of the laminate to transfer shear stress within two interfaces: laminate-support and between laminate layers.

In the spirit of the Eurocodes classification for steel joints, an analogous distinction should be proposed for the laminate systems, divided into rigid systems,

21

368 partial-dissipative systems and and dissipative systems. The rigid FR systems induce failure of the support element without shear-slip dissipation. Conversely,

370 the partial-dissipative FR systems are able to dissipate energy through shear interface energy but without inducing failure at the support. Finally, dissipative

372 FR systems are characterized by a high shear interface energy dissipation which generates laminate detachment or debonding. With this proposed approach,

374 specimens C belong to the rigid FR systems whereas specimens A are dissipative systems. So the failure mode encounter in our experimental test is able to

376 define the weak element of the FR system: support, laminate or laminate layers interface.

378 For the beam-test schedule, in the case of rigid FR systems, the design shear formula given by [37], for the shear traction strength criteria of beam element

$$V_{Rsd} = z\frac{A_{sw}}{s}f_{yd}[\cot(\alpha) + \cot(\theta)]\sin(\alpha)$$

380 has been used to predict the specimen C ultimate load for concrete shearing, where z, A_{sw}, s, f_{yd}, α and θ represent the internal lever arm, the transverse re-

382 bars cross section area, the rebars span, the rebars yield design tensile strength, the angles of the rebars orientation and of the idealized compressive concrete

384 element (by means of Morsch resistance criteria) with respect to the longitudinal bars respectively. The only change made on this formula is the substitution

386 of the internal level arm value $z = 0.9d$ with

$$z = \min\{0.9d; L_A\}, \tag{2}$$

where d is the difference between the cross section height and the concrete cover.

388 As reported in Table 4, in terms of design formula relative error,

$$\epsilon_{P_{MAX}} = \frac{P_{u,M-NTC} - P_{MAX,test}}{P_{u,M-NTC}} \tag{3}$$

the ultimate load predicted by the rearranged [37] formula provides a self-

390 confident results nearly always.

Conversely, for low strength matrix-fibre interfaces as for specimens A, dis-

392 sipative FR system, [42] proposed an upper limit for the ultimate debonding

22

force, based on the shear energy computing,

$$P_{dbu} = \sqrt{2 p_f E_f A_f G_f} \qquad (4)$$

where E_f, A_f and G_f denote the Young modulus, section area and interface fracture energy of the wire fabric, respectively, whereas $p_f = b$.

4. Peeling influence

The laminates ultimate forces P_u have been reported in Figure 6 with respect to the lamination length. For the case of specimen A, the behaviour is really close to some behaviours reported in [19, 42, 43, 44] for both FRPs and FRCMs bonded to concrete support, but not argued. Our results, as well as some other Literature results seem to suggest that over a certain lamination length the ultimate force decreases [1]. This curious behaviour might be due to the complex contact interface mechanical interaction between shear (τ) and peeling stresses (q) investigated in the following.

The mechanical interaction between a thin layer bonded to a substrate allows understanding why the ultimate force of a composite bonded to a concrete support tends to decrease over a certain lamination length. The analytical studies performed in [33, 34] describe the mechanical interaction between a cover and an elastic substrate taking into account both the peeling and shear stresses $q - \tau$.

Let us consider the beam-substrate interaction representative of a thin laminate bonded to a concrete support. The key point is to analyse how the stiffness of the covering (laminate) with respect to the support stiffness can influence the interface mechanical interaction. In particular, the superposition of two loading

---

[1] The authors are aware that such behaviour can be attributed to a swing of data that, in essence, would correspond to a plateau. But, recent MhBT and double lap tests, done at lower displacement rate, as performed by [45], suggest that at higher displacement rate, higher lamination lengths could reduce the system strength due to geometric aspects.

cases discussed in [34], namely a symmetric and skew-symmetric pair of axial
416 forces acting at the beam edges, is significant to clarify this aspect.

The problem is governed by a dimensionless parameters $E_s\chi_l/G_l$ and the
418 laminate slenderness ratio t/L, as observed by [34] yet, where χ and G are the
shear factor and shear elastic modulus. The subscript l and s will be used to
420 denote laminate and substrate quantities, respectively. The case of a single
force acting at the right beam edge is reported in Figure 12(a). Hence, for
422 this loading condition, the ratio between the interfacial peel and shear stresses
has been reported in Figure 12(b) vs the dimensionless horizontal coordinate
424 $\xi = x/L$ centred at the middle span of the laminate. In Figure 12(b), the
darker grey areas represents the region in which the strength of the interface is
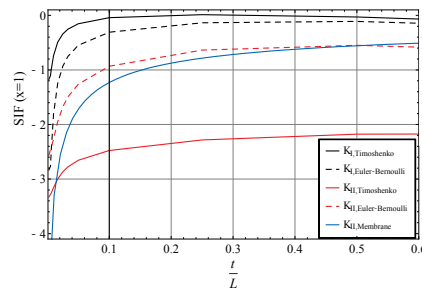promoted. Indeed, a positive peeling-tau ratio means that peeling component
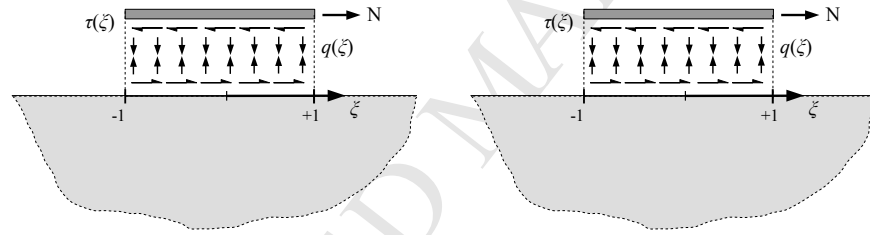
(a) Mechanical interaction reference system, with $E_s = E_l$, $\nu_s = \nu_l$.

(b) Interaction diagram
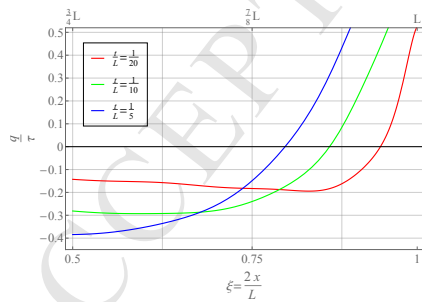
(c) Influence of laminate slenderness ratio in the neighbourhood of loading point

(d) Stress intensity factor for different model assumptions.

Figure 12: Mechanical interaction, peeling-shear stress ratio from [34] method, with $E_s = E_l$ and $\nu_l = \nu_s = 0.21$.

426

24

plays a beneficial effect on the shear strength by supplying compression. Hence

428 the laminate-substrate detachment, which always starts from the region closer to the loading point, turns up to be inhibited by the peeling stress component.

430 As the laminate slenderness ratio increases, the inversion point (IP), i.e. the point closer to the loading point where the mechanical interaction ratio (q/τ)

432 changes in sign, moves to the left and, in turn, both the regions characterized by the maximum compressive peeling stresses increase, Figure 12(c). This means

434 that, for high laminate slenderness ratios, the composite system increases significantly its debonding strength. Figure 12(c) highlights that despite of the

436 commonly assumption of negligible peeling stress, the peeling stress component is able to achieve values higher than the 10% of the shear component. The ulti-

438 mate load decreases as a critical lamination length is exceeded, thus suggesting that an optimal compromise between the materials strength and the q/τ interac-

440 tion exists. As a consequence, once the geometry and the materials parameters (in particular, the laminate thickness, interface peeling and shear strength) are

442 known as well the pure shear and peeling strength, the optimal bond length can be assessed. The analytical model allows evaluating how the laminate affects

444 the failure mode of the system. By assuming three different models for the laminate, i.e. Timoshenko beam, Euler-Bernoulli beam and truss element, the stress

446 intensity factors (SIFs) at the loading edge have been reported in Figure 12(d) varying t/L. As expected, the problem is governed by mode II, even if the mode

448 I is not negligible with respect mode II.

5. Conclusions

450 An experimental investigation about beam-test on two different types of wire fabric with DIC monitoring has been performed. Through the post-processing of

452 DIC data the specimen behaviour in terms of force-displacement curves, slippage distribution within the contact region and related energy as well as fracture

454 opening have been discussed. The following conclusion can be drawn:

- the load transfer performance of wire fabrics A and C differ in terms of fail-

25

456 ure mode. Adhesive fracture has been observed for specimens with fabric type A, which exhibit a pure friction strength mechanism based on slip-
458 page between the laminate layers, thus giving an almost linear ascending or plastic force-slip curve. Conversely, specimens C could take advantage
460 of an extra mechanical strength provided by a high mesh spacing affecting the employment index, as reported in Table 5;

462 • the vacuum thrust failure mode plays a crucial role only for sample C_1. This kind of failure indicates a good laminate-substrate shear transfer
464 attitude, which allow to achieve high performance by the increase of lamination length. We suppose that, when vacuum thrust failure occurs, an
466 increase of the lamination length produces failures into the support, as exhibited by samples C_2 and C_3. Hence the MhBT set-up might be more
468 suitable to investigate the mechanical behaviour of a composite system in which the lamination length exceeds the beam height minus the height
470 of the hinge device to avoid vacuum trust failure. In order to better understand the results provided by MhBT compared with the other tests
472 schedules shown in Figure 1, a further experimental program based on double lap and other beam-test, reducing the displacement rate, are in
474 progress;

• The results provided by fracture opening plot, Figure 11, suggest to use
476 a safety factor aimed at preventing the crack formation ranging between 0.5-0.7 (the serviceability load level). In addition for specimens C, the
478 modified Italian design formula [37], based on the common Morsch truss strength mechanism provides a good design formula for beam-test results;

480 • the analytic model proposed by [34] highlights that fixed the elastic material constants, the laminates with low values of slenderness promote the
482 debonding strength. This fact, as discussed in Section 4, confirms the observed results, from which it can be state that over a certain lamination
484 length the ultimate force decreases;

26

- the proposed FR classification, i.e. rigid systems, partial dissipative sys-
tems and dissipative systems allows identifying the sacrificial element in
order to obtain a given behaviour of the system. In addition, this classifi-
cation could guide on design formula as a function of the governing failure
mode.

Acknowledgements

References

[1] M. Gesoglu, E. Güneyisi, G. F. Muhyaddin, D. S. Asaad, Strain hardening ultra-high performance fiber reinforced cementitious composites: Effect of fiber type and concentration, Composites Part B: Engineering 103 (2016) 74–83.

[2] İ. Şanal, N. Özyurt, A. Hosseini, Characterization of hardened state behavior of self compacting fiber-reinforced cementitious composites (SC-FRCC's) with different beam sizes and fiber types, Composites Part B: Engineering 105 (2016) 30–45.

[3] R. Barretta, F. M. De Sciarra, M. Diaco, Small-scale effects in nanorods, Acta Mechanica 225 (7) (2014) 1945–1953.

[4] R. Barretta, F. M. de Sciarra, Analogies between nonlocal and local Bernoulli-Euler nanobeams, Archive of Applied Mechanics 85 (1) (2015) 89–99.

[5] G. Romano, R. Barretta, M. Diaco, F. M. de Sciarra, Constitutive boundary conditions and paradoxes in nonlocal elastic nanobeams, International Journal of Mechanical Sciences 121 (2017) 151–156.

27

[6] L. Lanzoni, A. Nobili, A. Tarantino, Performance evaluation of a polypropylene-based draw-wired fibre for concrete structures, Construction and Building Materials 28 (1) (2012) 798–806.

[7] A. Nobili, F. O. Falope, Impregnated carbon fabric–reinforced cementitious matrix composite for rehabilitation of the Finale Emilia hospital roofs: Case study, Journal of composites for construction 21 (4) (2017) 05017001.

[8] D.-Y. Yoo, N. Banthia, Y.-S. Yoon, Predicting service deflection of ultra-high-performance fiber-reinforced concrete beams reinforced with GFRP bars, Composites Part B: Engineering 99 (2016) 381–397.

[9] A. Caratelli, S. Imperatore, A. Meda, Z. Rinaldi, Punching shear behavior of lightweight fiber reinforced concrete slabs, Composites Part B: Engineering 99 (2016) 257–265.

[10] K. K. Choi, P. Meshgin, M. M. R. Taha, Shear creep of epoxy at the concrete-FRP interfaces, Composites Part B: Engineering 38 (5) (2007) 772–780.

[11] F. Germano, G. Tiberti, G. Plizzari, Experimental behavior of SFRC columns under uniaxial and biaxial cyclic loads, Composites Part B: Engineering 85 (2016) 76–92.

[12] C. Carloni, K. V. Subramaniam, Investigation of sub-critical fatigue crack growth in frp/concrete cohesive interface using digital image analysis, Composites Part B: Engineering 51 (2013) 35–43.

[13] L. Dezi, A. M. Tarantino, Time-dependent analysis of concrete structures with a variable structural system, ACI Materials Journal 88 (3).

[14] L. Dezi, G. Menditto, A. M. Tarantino, Viscoelastic heterogeneous structures with variable structural system, Journal of Engineering Mechanics 119 (2) (1993) 238–250.

28

[15] L. Dezi, G. Menditto, A. M. Tarantino, Homogeneous structures subjected to repeated structural system changes, Journal of Engineering Mechanics 116 (8) (1990) 1723–1732.

[16] A. Nobili, C. Signorini, On the effect of curing time and environmental exposure on impregnated carbon fabric reinforced cementitious matrix (CFRCM) composite with design considerations, Composites Part B: Engineering 112 (2017) 300–313.

[17] L. Bizindavyi, K. Neale, Transfer lengths and bond strengths for composites bonded to concrete, Journal of composites for construction 3 (4) (1999) 153–160.

[18] T. D' Antino, C. Carloni, L. Sneed, C. Pellegrino, Matrix–fiber bond behaviour in PBO FRCM composites: A fracture mechanics approach, Engineering Fracture Mechanics 117 (2014) 94–111.

[19] J. Yao, J. Teng, J. Chen, Experimental study on FRP-to-concrete bonded joints, Composites Part B: Engineering 36 (2) (2005) 99–113.

[20] F. Bencardino, A. Condello, A. F. Ashour, Single-lap shear bond tests on steel reinforced geopolymeric matrix-concrete joints, Composites Part B: Engineering 110 (2017) 62–71.

[21] M. R. Valluzzi, D. V. Oliveira, A. Caratelli, G. Castori, M. Corradi, G. De Felice, E. Garbin, D. Garcia, L. Garmendia, E. Grande, et al., Round robin test for composite-to-brick shear bond characterization, Materials and Structures 45 (12) (2012) 1761–1791.

[22] L. De Lorenzis, B. Miller, A. Nanni, Bond of fiber-reinforced polymer laminates to concrete, ACI Materials Journal 98 (3) (2001) 256–264.

[23] L. Ombres, Debonding analysis of reinforced concrete beams strengthened with fibre reinforced cementitious mortar, Engineering Fracture Mechanics 81 (2012) 94–109.

29

[24] A. Meda, F. Minelli, G. A. Plizzari, Flexural behaviour of RC beams in fibre reinforced concrete, Composites Part B: Engineering 43 (8) (2012) 2930–2937.

[25] J. Ghen, Z. Yang, G. Holt, FRP or steel plate-to-concrete bonded joints: Effect of test methods on experimental bond strength, Steel & Composite Structures 1 (2) (2001) 231–244.

[26] H. Yuan, W. Wu, H. Yoshizawa, Theoretical solutions on interfacial stress transfer of externally bonded steel/composite laminates., Journal of Structural Mechanic Erthquake Engineering I (675) (2001) 27–39.

[27] X. Lu, J. Teng, L. Ye, J. Jiang, Bond–slip models for FRP sheets/plates bonded to concrete, Engineering structures 27 (6) (2005) 920–937.

[28] O. Büyüköztürk, T.-Y. Yu, Understanding and assessment of debonding failures in FRP-concrete systems, in: Seventh International Congress on Advances in Civil Engineering, Istanbul, Turkey, Citeseer, 2006, pp. 1–22.

[29] D. Corr, M. Accardi, L. Graham-Brady, S. Shah, Digital image correlation analysis of interfacial debonding properties and fracture behavior in concrete, Engineering Fracture Mechanics 74 (1) (2007) 109–121.

[30] W. C. Choi, S. J. Jang, H. D. Yun, Bond and cracking behavior of lap-spliced reinforcing bars embedded in hybrid fiber reinforced strain-hardening cementitious composite (SHCC), Composites Part B: Engineering 108 (2017) 35–44.

[31] A. M. Tarantino, Crack propagation in finite elastodynamics, Mathematics and Mechanics of Solids 10 (6) (2005) 577–601.

[32] A. M. Tarantino, Nonlinear fracture mechanics for an elastic Bell material, The Quarterly Journal of Mechanics and Applied Mathematics 50 (3) (1997) 435–456.

[33] P. Di Maida, F. O. Falope, Euler-Bernoulli nanobeam welded to a compressible semi-infinite substrate, Modelling and Simulation in Engineering 2016 (2016) 4.

[34] L. Lanzoni, E. Radi, A loaded Timoshenko beam bonded to an elastic half plane, International Journal of Solids and Structures 92 (2016) 76–90.

[35] K. Hannawi, H. Bian, W. Prince-Agbodjan, B. Raghavan, Effect of different types of fibers on the microstructure and the mechanical behavior of ultra-high performance fiber-reinforced concretes, Composites Part B: Engineering 86 (2016) 214–220.

[36] RILEM TC, RC 5 Bond test for reinforcement steel. 1. Beam test, E & FN SPON, 1982.

[37] Ministero delle Infrastrutture, Consiglio Superiore dei Lavori Pubblici, D.M. 14/01/08. Norme tecniche per le costruzioni (NTC2008), Italian Official Bullettin 29.

[38] UNI EN, Methods of test for mortar for masonry - Determination of flexural and compressive strength of hardened mortar., UNI EN Standard.

[39] ACI Committee 549.1R-93, Guide for the design, construction, and repair of ferrocement, American Concrete Institute.

[40] DT200 CNR, Guide for the design and construction of an externally bonded FRP system for strengthening existing structures, Italian National Research Council, Rome.

[41] A. D'Ambrisi, L. Feo, F. Focacci, Experimental and analytical investigation on bond between carbon-FRCM materials and masonry, Composites Part B: Engineering 46 (2013) 15–20.

[42] A. D'Ambrisi, L. Feo, F. Focacci, Experimental analysis on bond between PBO-FRCM strengthening materials and concrete, Composites Part B: Engineering 44 (1) (2013) 524–532.

31

[43] J. Chen, J. Teng, Anchorage strength models for FRP and steel plates bonded to concrete, Journal of Structural Engineering 127 (7) (2001) 784–791.

[44] T. Maeda, Y. Asano, Y. Sato, T. Ueda, Y. Kakuta, A study on bond mechanism of carbon fiber sheet, in: Non-Metallic (FRP) Reinforcement for Concrete Structures, Proceedings of the Third Symposium, Vol. 1, 1997, pp. 279–286.

[45] C. Carloni, S. Verre, L. H. Sneed, L. Ombres, Loading rate effect on the debonding phenomenon in fiber reinforced cementitious matrix-concrete joints, Composites Part B: Engineering 108 (2017) 301–314.